11th International Symposium on Turbulence and Shear Flow Phenomena (TSFP11)
Southampton, UK, July 30 to August 2, 2019

MODAL ANALYSIS OF COHERENT STRUCTURES IN A SELF-SIMILAR TURBULENT BOUNDARY LAYER WITH ADVERSE PRESSURE GRADIENT

Jens S. Müller, Kilian Oberleithner
Laboratory for Flow Instabilities and Dynamics
Institut für Strömungsmechanik
und Technische Akustik
Technische Universität Berlin
10623 Berlin, Germany
jens.mueller@tu-berlin.de

Atsushi Sekimoto
Division of Chemical Engineering
Department of Materials Engineering Science
Graduate School of Engineering Science,
Osaka University
Toyonaka, Osaka 560-8531, Japan

Michael P. Eisfelder, Abel-John Buchner,
Vassili Kitsios, Callum Atkinson, Julio Soria
Laboratory for Turbulence Research in Aerospace and Combustion
Department of Mechanical and Aerospace Engineering
Monash University
Melbourne, Victoria 3800, Australia

ABSTRACT

Local linear stability analysis as well as Fourier transform and proper orthogonal decomposition are applied to a self-similar turbulent boundary layer on a flat plate with strong adverse pressure gradient to identify coherent structures. The modal analysis is based on data from direct numerical simulations. Coherent structures are identified at the wall-normal position that coincides with an inflection point in the streamwise mean velocity profile. It is found that these coherent structures are governed by broadband Kelvin–Helmholtz instabilities, which are linearly unstable for a certain self-similar frequency range, leading to spatial amplification in streamwise direction before they decay downstream.

A very particular challenge is faced due to the limited time length of the dataset compared to the characteristic timescales of interest. Likewise, the spatial extent in streamwise direction limits the large observable wavelengths of interest. This issue is coped with by applying a Fourier transform in time combined with subsequent proper orthogonal decompositions in streamwise and spanwise direction to extract the statistically most correlated and coherent modes in the turbulent boundary layer.

INTRODUCTION

Turbulent boundary layers (TBL) in adverse pressure gradients (APG) are highly relevant in engineering flows such as airfoils. They are responsible for the additional increase of drag related to the significant growth of boundary layer thickness.

Direct numerical simulations (DNS) have been conducted on a flat plate for a strong APG TBL at self-similar conditions (Kitsios *et al.*, 2017). The Reynolds numbers based on the displacement thickness δ_1 in the self-similar domain is $Re_{\delta_1} = 22\,200$ to $28\,800$. The nondimensional streamwise pressure gradient parameter $B = \delta_1 \, (\partial p/\partial x) \, / \, \tau_w$, with streamwise pressure gradient $\partial p/\partial x$ and wall shear stress τ_w, was set to $B = 39$ to simulate a strong APG close to the verge of separation.

Fjørtoft's theorem states that a necessary condition for the occurrence of Kelvin–Helmholtz (KH) instabilities is the existence of an inflection point in the streamwise base velocity profile that is simultaneously accompanied by a maximum of spanwise vorticity (Schmid & Henningson, 2012). For the strong APG an inflection point satisfying Fjørtoft's criterion can be found at $y/\delta_1 = 1.1$, as marked in Fig. 1 in the streamwise mean velocity profile.

An examination of the Reynolds stresses further hints at the action of a KH instability mechanism. The spanwise turbulent shear stress $\overline{u'v'}$ as well as the the streamwise turbulent normal stress $\overline{u'^2}$ peak around $y/\delta_1 \approx 1.1$ (not shown here). At this position the inflection point is located. Further studies additionally support this notion and suggest that the outer region of the boundary layer can be regarded as a free shear layer when a strong APG is present (e.g. Kitsios *et al.* (2017); Schatzman & Thomas (2017); Harun *et al.* (2013)).

Since the range of turbulence scales is in general very large, particularly in high Reynolds number flows, it is difficult to 'cleanly' extract these coherent structures. The goal of this paper is to present a modal analysis approach that identifies the coherent structures inside the boundary layer. A local linear stability analysis (LSA) is performed that provides the eigenmodes of the mean flow. The results are compared to the structures extracted directly from the snapshots of the flow field by a combination of a Fourier transform (FT) in time and proper orthogonal decompositions (POD) in space.

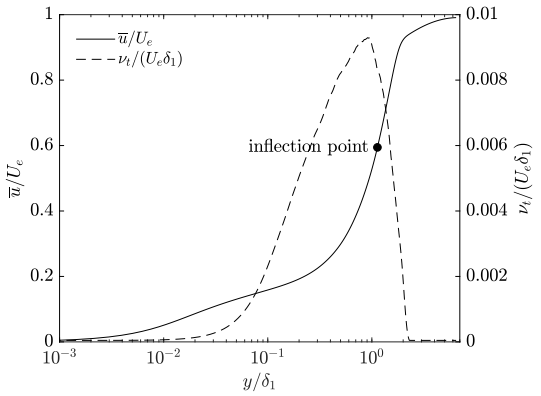

Figure 1: Mean velocity profile of the streamwise component $\overline{u}/U_e$ and modeled eddy viscosity $\nu_t/(U_e\delta_1)$ as a function of wall-normal coordinate y/δ_1

METHODS & DATA ANALYSIS

Coherent structures can be described by a triple decomposition (Reynolds & Hussain, 1972). Let $\mathbf{q}(\mathbf{x},t) = [\mathbf{u},p]^\top$ be the summarized vector of the flow velocity vector $\mathbf{u}$ and the pressure p. $\mathbf{q}$ can then be decomposed by $\mathbf{q}(\mathbf{x},t) = \overline{\mathbf{q}}(\mathbf{x}) + \widetilde{\mathbf{q}}(\mathbf{x},t) + \mathbf{q}''(\mathbf{x},t)$, where $\overline{\mathbf{q}}$ is the time-averaged mean part, $\widetilde{\mathbf{q}}$ is the coherent part and $\mathbf{q}''$ is the stochastic part.

Linear stability analysis

The coherent part of a parallel turbulent flow can be modeled by a local LSA, at least when the coherent structures are constituted by linear eigenmodes. The LSA of turbulent flows is based on the Navier–Stokes equations of the coherent fluctuation $\widetilde{\mathbf{q}}$ linearized around the mean flow $\overline{\mathbf{q}}$ (Reynolds & Hussain, 1972):

$$\frac{\partial\widetilde{\mathbf{u}}}{\partial t} + \widetilde{\mathbf{u}}\cdot\nabla\overline{\mathbf{u}} + \overline{\mathbf{u}}\cdot\nabla\widetilde{\mathbf{u}} = -\frac{\nabla\widetilde{p}}{\rho} + \nabla\cdot\left(\nu\left(\nabla+\nabla^\top\right)\widetilde{\mathbf{u}}\right) - \nabla\cdot\widetilde{\mathbf{u}''\mathbf{u}''} \quad (1)$$

$$\nabla\cdot\widetilde{\mathbf{u}} = 0. \quad (2)$$

For the solution only normal modes are used as an ansatz of the form $\widetilde{\mathbf{q}}(\mathbf{x},t) \propto \hat{\mathbf{q}}(y)\mathrm{e}^{\mathrm{i}(\alpha x+\beta z-\omega t)} + \text{c.c.}$ Here, x is the streamwise, y is the wall-normal and z the spanwise coordinate. α and β denote the angular streamwise and spanwise wavenumbers, respectively, and ω denotes the angular frequency. $\hat{\mathbf{q}}$ is the complex amplitude. The spanwise wavenumber is set to $\beta = 0$ since it is later determined that most of the coherent energy is contained at $\beta = 0$ and other very low spanwise wavenumbers. By specifying a range of frequencies ω, an eigenvalue problem for each frequency is obtained. The solutions provide the eigenmodes with their respective streamwise wavenumbers α_r and convective growth rates $-\alpha_i$. The discretized eigenvalue problem is solved by using a Chebyshev spectral collocation method similar to Khorrami *et al.* (1989), but implemented for Cartesian coordinates and a spatial analysis. The mean flow profile is extended with constant value into the farfield to $y/\delta_1 = 50$ and homogeneous Dirichlet conditions for the velocities at the wall and in the farfield are imposed. For the pressure, homogeneous Neumann conditions are set at the wall and in the farfield.

Equations 1 and 2 are not closed since $\widetilde{\mathbf{u}''\mathbf{u}''}$ is unknown. This term describes the interaction between coherent and stochastic field due to the perturbation of the stochastic Reynolds stresses by a coherent wave. This interaction can be modeled with a Boussinesq approximation,

$$\widetilde{\mathbf{u}''\mathbf{u}''} = -\nu_t\left(\nabla+\nabla^\top\right)\widetilde{\mathbf{u}}, \quad (3)$$

in which only the unknown eddy viscosity ν_t needs to be determined. Here, the eddy viscosity is obtained via a least-square fit over the turbulent Reynolds stress tensor and mean strain rate (Ivanova *et al.*, 2013). The calculated eddy viscosity peaks around the inflection point and reaches close to the wall (see Fig. 1).

Empirical mode decomposition

A typical approach to extract broadband coherent structures directly from the snapshots is to apply the frequency-domain (or wavenumber-domain) spectral POD as originally proposed by Lumley (1967). In essence, the spectral POD is based on the correlation of temporal (or spatial) Fourier coefficients at a given frequency (or wavenumber). These Fourier coefficients are obtained by segmenting the complete dataset into a number of subsets where each segment is assumed to be a statistically independent realization of the flow. In the present dataset, any segmentation in time (or space) prior to conducting a FT in order to facilitate a spectral POD would be detrimental to the lowest resolvable frequency (or lowest resolvable wavenumber) which is why this approach is not followed here. Instead, the following four main steps are performed as sketched in Fig. 2. The steps comprise 1) transforming the snapshots into self-similar coordinates, 2) applying a FT in time, 3) applying a classical snapshot POD (Berkooz *et al.*, 1993) on the temporal Fourier coefficients in streamwise direction and 4) applying a snapshot POD on the leading x-POD mode in spanwise direction.

In the first step, all variables are nondimensionalized by the length scale δ_1, the velocity scale U_e (corresponding to the maximum outer velocity at the upper end of the boundary layer) and the time scale δ_1/U_e, rendering the flow self-similar. If not emphasized otherwise within the text, all mentioned quantities are nondimensional, e.g. when a frequency or wavelength is discussed, the nondimensional frequency or nondimensional wavelength is implied. Dimensional quantities within the text are stated explicitly.

In the second step, a FT in time is applied to the snapshots. From the obtained temporal Fourier coefficients, only the nondimensional frequencies at the lower end of the resolvable spectrum are considered, ranging from $f\delta_1/U_e = 0.19$ to 1.47, since these contain most of the energy. Furthermore, at every cross-section along x, all data points $(y/\delta_1, z/\delta_1)$ are discarded that do not intersect with the $(y/\delta_1, z/\delta_1)$-coordinates given by the most downstream cross-section at the end of the domain.

In the third step, a POD is performed on the temporal Fourier coefficients. The POD provides energy-optimal modes in which the temporal Fourier coefficients at a considered frequency correlate most optimal in x-direction. The results show that the leading mode is dominant compared to all remaining modes at a fixed frequency. At the lowest resolvable frequency $f\delta_1/U_e = 0.19$ the leading mode contains almost 40% of the energy (for this

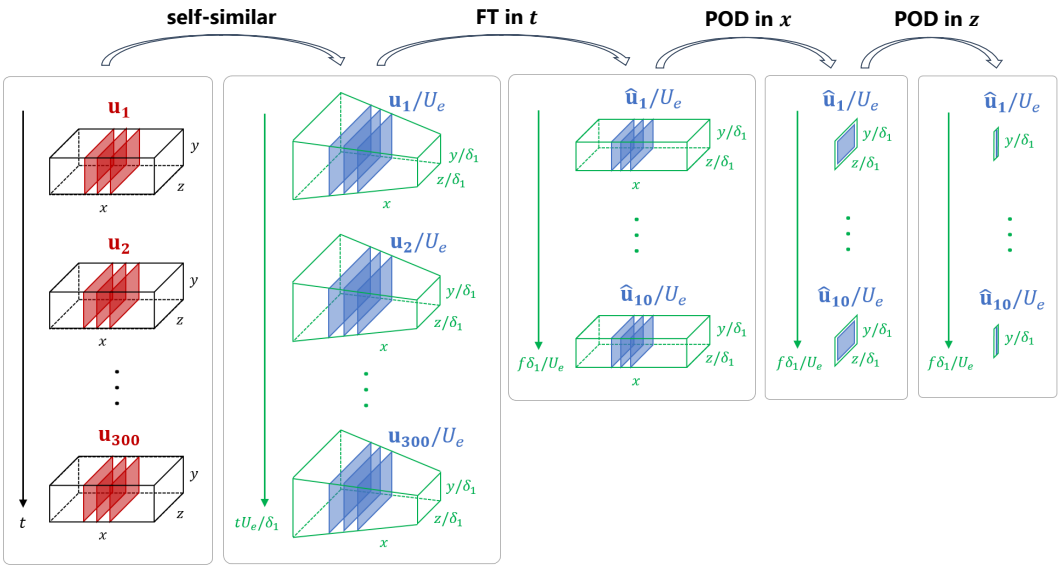

Figure 2: Schematic of empirical FT-POD analysis: 1) transforming snapshots into self-similar coordinates, 2) apply FT in time t to obtain temporal Fourier coefficients, 3) apply POD in streamwise direction x on temporal Fourier coefficients, 4) apply POD in spanwise direction z/δ_1 on leading x-POD mode

Fourier coefficient), while at the highest frequency the leading mode still contains almost 10% (not shown here for brevity). The POD also yields the corresponding POD space coefficients that reveal the fluctuations of the modes in x-direction. The coefficient of the leading mode shows a strong harmonic correlation. For this reason, the local streamwise wavelength can be obtained by differentiating the instantaneous phase angle along x. The dimensional streamwise wavelength λ_x slightly increases in dimensional x-direction. Scaling the dimensional wavelength with the local displacement thickness $\delta_1(x)$ results in an approximately constant nondimensional wavelength λ_x/δ_1. In this way, every leading POD mode can be attributed to a particular pair of nondimensional frequency and nondimensional streamwise wavelength.

As a last step, after conducting the POD in x-direction, a subsequent POD in z/δ_1-direction is performed on the leading modes at every given frequency. A regular FT is conducted on the spanwise POD space coefficients in order to reveal the spanwise wavelengths (or wavenumbers) that are prevalent in the POD modes.

The streamwise growth and decay rates of the structures can be inferred by exploiting the self-similarity property. The amplitude spectrum of the temporal Fourier coefficients depends on the nondimensional frequency $f\delta_1(x)/U_e(x)$ which is only a function of dimensional frequency f and dimensional streamwise coordinate x. $\delta_1(x)/U_e(x)$ increases monotonously with x (Kitsios *et al.*, 2017). Therefore, when a fixed *dimensional* frequency is given, the *nondimensional* frequency is proportional to x. Due to that equivalence, the streamwise growth and decay is simply determined by differentiating the amplitudes with respect to x.

The results after going through the entire process of conducting a FT in time, followed by a POD on the temporal Fourier coefficients in x-direction and a POD on the leading mode in z/δ_1-direction will simply be called Fourier Transform-Proper Orthogonal Decomposition (FT-POD) in the following.

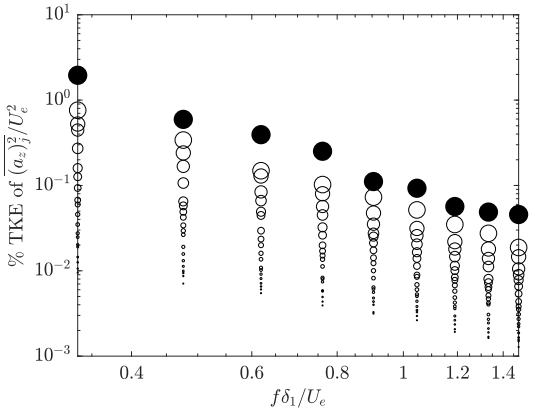

Figure 3: Relative percentage of total turbulent kinetic energy (TKE) of the POD space coefficients $\overline{(a_z)_j^2}/U_e^2$ as a function of frequency $f\delta_1/U_e$ (circle size denotes POD mode rank, i.e. largest circle is leading mode; leading mode is additionally denoted by filled marker)

RESULTS

Figure 3 shows the turbulent kinetic energy (TKE) of the POD space coefficients after performing the entire FT-POD. The large-scale structures at low frequencies contain the most energy compared to the smaller scales at higher frequencies. For each frequency, the leading POD mode has approximately twice as much TKE than the second-ranked mode. Remarkably, the leading mode at the lowest resolvable frequency holds almost 7% of the total TKE. This observation as well as the gap between leading and second-ranked POD mode indicate that a strongly coherent structure exists, justifying to focus on the leading modes in the following.

Figure 4 shows the amplitude spectrum of the leading FT-POD modes for the coherent wall-normal velocity component $\widetilde{v}$. The spectrum for the coherent streamwise component $\widetilde{u}$ is very similar and not shown here for brevity. Equal to Fig. 3, the highest amplitudes are contained at

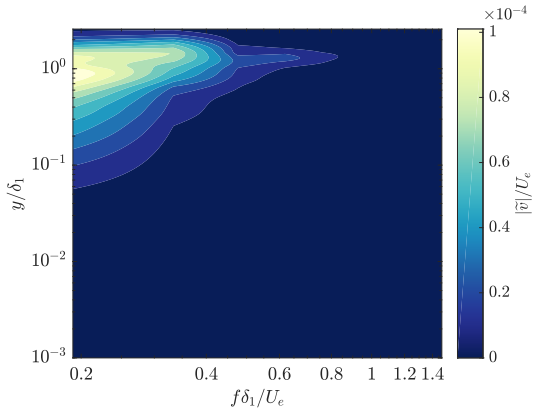

Figure 4: Amplitude spectrum of the leading FT-POD modes as a function of wall-normal coordinate y/δ_1 and frequency $f\delta_1/U_e$ for wall-normal coherent velocity $|\widetilde{v}|/U_e$

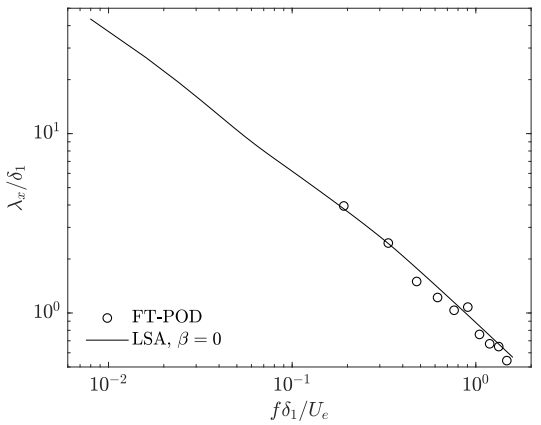

Figure 5: Streamwise wavelength λ_x/δ_1 of the leading FT-POD mode as a function of frequency $f\delta_1/U_e$

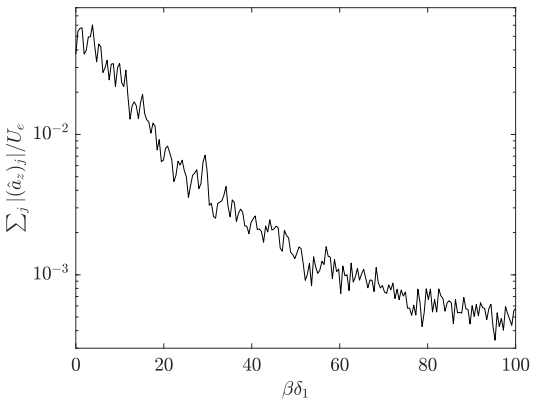

Figure 6: Spanwise wavenumber spectrum $\beta\delta_1$ of FT-POD integrated over entire resolved frequency range

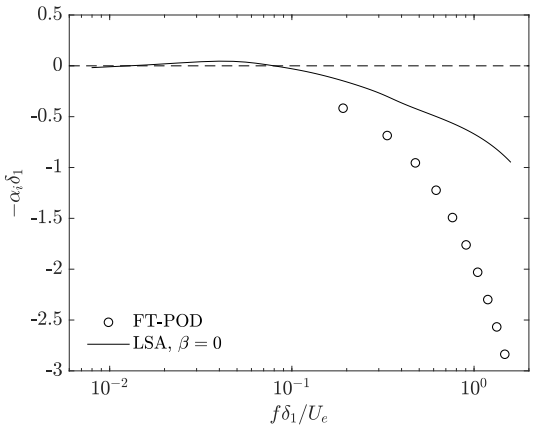

Figure 7: Streamwise convective growth rate $-\alpha_i\delta_1$ as a function of frequency $f\delta_1/U_e$ (dashed line denotes stability limit $-\alpha_i\delta_1 = 0$)

low frequencies. With increasing frequency, the amplitudes decrease significantly (note the linear color scale in contrast to the logarithmic axis scale in Fig. 3). Prominently, the highest amplitudes accumulate around $y/\delta_1 \approx 1$, which coincides with the inflection point position at $y/\delta_1 = 1.1$. This suggests a correlation between the concentrated strong amplitude at the inflection point and the compliance to Fjørtoft's criterion, potentially supporting KH-type instabilities. It needs to be emphasized that the spectrum shown here is the result of a significantly narrowing 'condensation' of the spectral content of the entire spatio-temporal dataset after applying the FT in time and spatial POD in x and z/δ_1. The amplitudes observed here correspond to a single frequency and a single streamwise wavelength as well as a dominant bandwidth of spanwise wavenumbers (both discussed in the next paragraph). Therefore, the modes investigated here can indeed be considered coherent in space and time, representing distinct wavepackets in the TBL.

Based on the POD space coefficients in x-direction the derived streamwise wavelengths λ_x/δ_1 are displayed in Fig. 5. With increasing frequency the streamwise wavelength decreases. In addition, the results from the local LSA for $\beta\delta_1 = 0$ are shown here for comparison. In the resolved frequency range of the FT-POD the match is excellent.

In Fig. 6 the spanwise wavenumber spectrum integrated over the entire resolved frequency range is shown. The POD coefficients do not show a preferable spanwise wavenumber. Evidently, the spectral content of the extracted FT-POD modes is dominated by the smallest spanwise wavenumbers around $\beta\delta_1 \approx 0$, i.e. the largest spanwise wavelengths.

The streamwise convective growth rate $-\alpha_i\delta_1$ is shown in Fig. 7. The empirical growth rate obtained by FT-POD clearly exhibits a convective decay of wavepackets in the resolved frequency range. This partly coincides with the LSA results which reveal a decay rate $+\alpha_i\delta_1$ in the same frequency range as well. However, the decay rates obtained by the LSA are increasingly underestimated for higher frequencies. This suggests that the eddy viscosity used for modeling the dissipation term in the LSA is progressively too low at the smaller scales. For the large scales, the derived eddy viscosity appears to be an appropriate model for the interaction between coherent and stochastic field, since the match between LSA and FT-POD at the lower end of the resolved frequency range is better. Thus, with smaller scales at higher frequencies, the eddy viscosity would need to be actually larger to account for the increasing dissipation.

For the very low frequencies, a range of actual convective growth is evident from the LSA results. That range is, however, not resolvable empirically due to the limited

length of the present dataset.

Based on these results, a governing mechanism in this flow is hypothesized as follows. Since the APG TBL is self-similar, the dependence of the nondimensional growth rate from the nondimensional frequency can be interpreted in several ways. One possibility is to interpret Fig. 7 for a fixed *dimensional* frequency $f = \text{const}$. Knowing that $\delta_1(x) \propto x$ and $U_e \propto x^{-0.23}$ (Kitsios *et al.*, 2017), the values on the abscissa can also be read to be proportional to x. Following this notion, this means that for a specific dimensional frequency, the structure of a supposed KH instability is convectively amplified in downstream direction at first for $-\alpha_i > 0$. Then, the structure grows in x-direction until it saturates at $-\alpha_i = 0$. Subsequently, the structure decays since $-\alpha_i < 0$.

With increasing dimensional frequency, the streamwise extent of spatial amplification is shifted farther upstream, such that growing and decaying wavepackets occur more upstream when they are small-scale (in dimensional units) and occur more downstream when they are large-scale. Note that this interpretation holds as long as the domain is infinitely long in upstream and downstream direction. This is implicitly assumed for self-similar flows.

Figure 8 and 9 compare the mode shapes of the coherent structure extracted by FT-POD to the mode shapes predicted by LSA. Due to the arbitrary amplitude scaling of eigenmodes in eigenvalue problems, the magnitude is normalized by the maximum magnitude to allow a direct comparison of the spatial structure. In every case, a very dominant peak around the inflection point at $y/\delta_1 = 1.1$ exists. However, there is a slight mismatch of the peak position. The LSA predicts the coherent structure to occur farther away from the wall than what is observed empirically by the FT-POD. Again, as for the underestimation of the decay rates, this may be related to the modeled eddy viscosity that peaks around the inflection point, inhibiting significant growth of the structure closer to the inflection point and, thus, closer to the wall. For the low frequencies $f\delta_1/U_e \leq 0.33$, the peak is comparably broad, indicating that the mode penetrates close towards the wall, down to at least $y/\delta_1 \approx 0.1$. For higher frequencies, the peak width narrows and the mode is more concentrated around the inflection point position. This can be observed in both FT-POD and LSA results. This is probably related to the smaller streamwise wavelengths, leading to smaller scales in wall-normal direction likewise.

CONCLUSION

Coherent structures are found to arise in the outer region of the TBL with strong APG. For very low nondimensional frequencies, the LSA predicts linearly unstable coherent structures with spatial growth in streamwise direction. The self-similarity allows for interpreting the nondimensional results for arbitrary *dimensional* frequencies at arbitrary x-positions. This constructs the picture of KH-type wavepackets that are spatially growing and decaying in streamwise direction in which smaller structures occur in upstream regions while larger structures occur farther downstream. This is in accordance with the displacement thickness δ_1 as a characteristic length scale increasing in downstream direction. For the present dataset, only the nondimensional frequency range of decaying modes is resolvable. Although the decay rates that are determined empirically by the FT-POD only qualitatively agree with the decay rates predicted by the LSA, the streamwise wavelengths agree well and the spatial mode shapes on an acceptable level between FT-POD and LSA.

To extend the discussion and improve the demonstrated model, the used eddy viscosity model would need to be revised. It was revealed that the mismatch of the decay rates and the mode shapes is strongly affected by the eddy viscosity and that the match deteriorates with increasing frequency. Therefore, instead of providing a scale-independent eddy viscosity, an eddy viscosity model being a function of frequency would have the potential to provide improved results. Based on the Boussinesq approximation in Eqn. 3 and the scale-decomposed FT-POD modes, the eddy viscosity could be calculated explicity for every frequency of interest and, subsequently, the LSA would be conducted with a frequency-varying eddy viscosity.

ACKNOWLEDGMENT

The authors would like to acknowledge the research funding by the Australian Government through the Australian Research Council and the Australia-Germany Joint Research Cooperation Scheme, an initiative of Universities Australia and the German Academic Exchange Service (DAAD).

REFERENCES

Berkooz, G., Holmes, P. & Lumley, J. L. 1993 The proper orthogonal decomposition in the analysis of turbulent flows. *Annual review of fluid mechanics* **25** (1), 539–575.

Harun, Z., Monty, J. P., Mathis, R. & Marusic, I. 2013 Pressure gradient effects on the large-scale structure of turbulent boundary layers. *Journal of Fluid Mechanics* **715**, 477–498.

Ivanova, E. M., Noll, B. E. & Aigner, M. 2013 A numerical study on the turbulent schmidt numbers in a jet in crossflow. *Journal of Engineering for Gas Turbines and Power* **135** (1), 011505.

Khorrami, M. R., Malik, M. R. & Ash, R. L. 1989 Application of spectral collocation techniques to the stability of swirling flows. *Journal of Computational Physics* **81** (1), 206–229.

Kitsios, V., Sekimoto, A., Atkinson, C., Sillero, J. A., Borrell, G., Gungor, A. G., Jiménez, J. & Soria, J. 2017 Direct numerical simulation of a self-similar adverse pressure gradient turbulent boundary layer at the verge of separation. *Journal of Fluid Mechanics* **829**, 392–419.

Lumley, John Leask 1967 The structure of inhomogeneous turbulent flows. *Atmospheric turbulence and radio wave propagation* .

Reynolds, W. C. & Hussain, A. K. M. F. 1972 The mechanics of an organized wave in turbulent shear flow. part 3. theoretical models and comparisons with experiments. *Journal of Fluid Mechanics* **54** (2), 263–288.

Schatzman, D. M. & Thomas, F. O. 2017 An experimental investigation of an unsteady adverse pressure gradient turbulent boundary layer: embedded shear layer scaling. *Journal of Fluid Mechanics* **815**, 592–642.

Schmid, P. J. & Henningson, D. S. 2012 *Stability and transition in shear flows*, , vol. 142. Springer Science & Business Media.

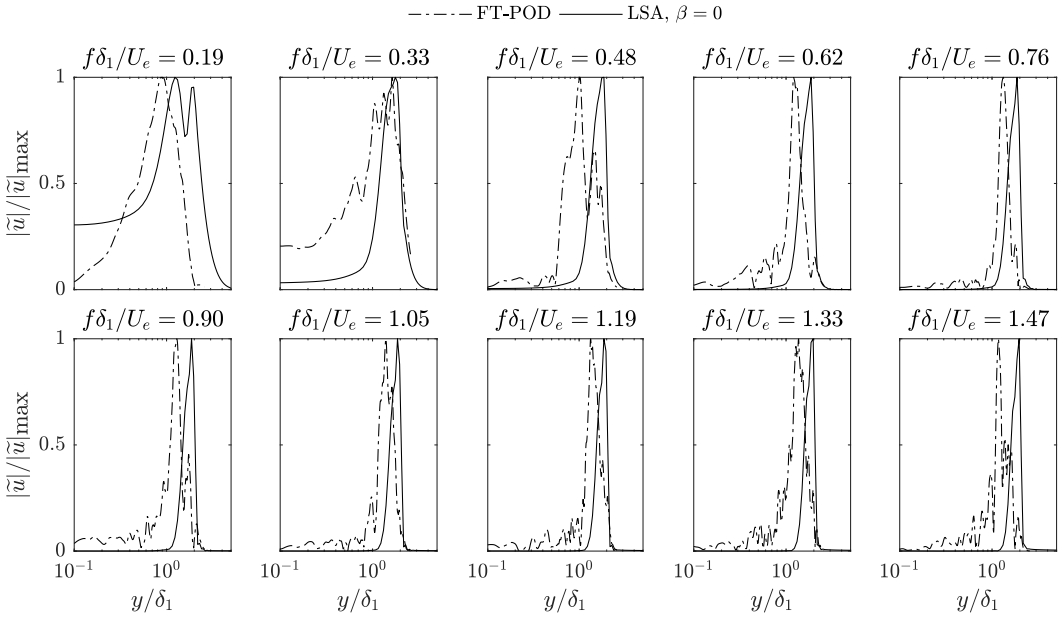

Figure 8: Mode shapes of streamwise coherent fluctuation $|\widetilde{u}|/|\widetilde{u}|_{\max}$ as a function of wall-normal coordinate y/δ_1 for different frequencies $f\delta_1/U_e$

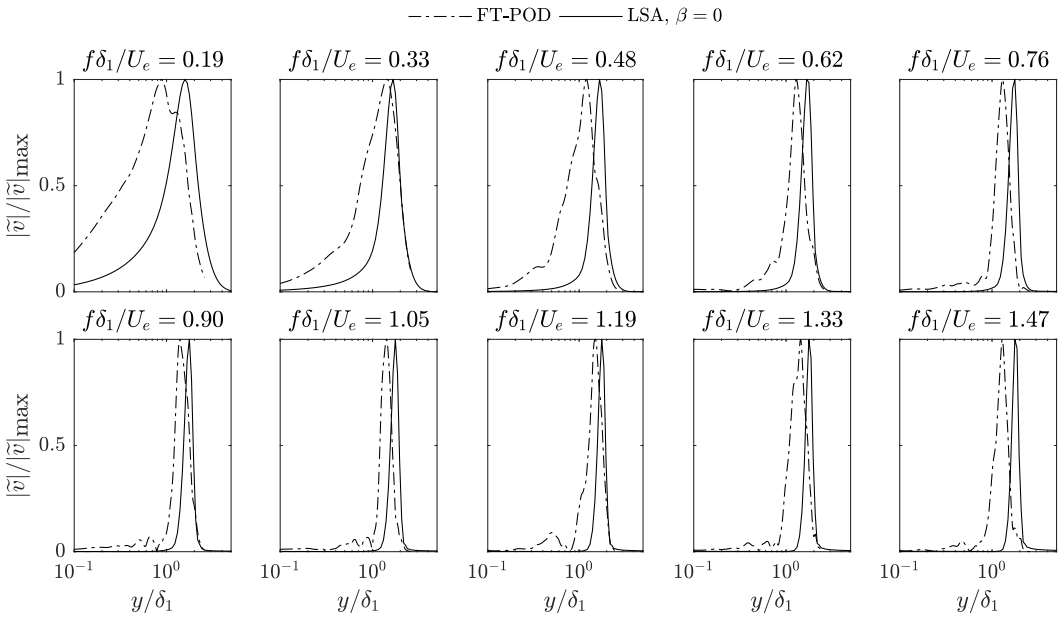

Figure 9: Mode shapes of wall-normal coherent fluctuation $|\widetilde{v}|/|\widetilde{v}|_{\max}$ as a function of wall-normal coordinate y/δ_1 for different frequencies $f\delta_1/U_e$